Supplementary Materials: The Impact of Lead Patterns on Mean Profiles of Wind, Temperature, and Turbulent Fluxes in the Atmospheric Boundary Layer over Sea Ice

Janosch Michaelis * and Christof Lüpkes
Alfred Wegener Institute Helmholtz Centre for Polar and Marine Research, 27570 Bremerhaven, Germany
* **Correspondence: janosch.michaelis@awi.de**

1. Horizontal Development of ABL Height Obtained by the Simulations NL-M20-zi and NL-LS96-zi

In this section, we show the atmospheric boundary layer (ABL) height z_i as a function of the distance to the downwind edge of the inflow region as considered in the model simulations using non-local closures in which we allow variations of z_i in flow direction (see Section 2.3.4 in the main manuscript). The corresponding results, which are from the model runs NL-M20-zi for the lead-resolving cases (ENS-1km, ENS-2km, ENS-5km-d20km, ENS-5km-d40km, and ENS-10km) and from the run NL-LS96-zi for the case ENS-C, are shown in Figure S1. The specifications of these model runs as well as an overview of the cases are provided in Section 2 of the main manuscript.

We consider variations of z_i in flow direction by diagnostically calculating this quantity with the so-called contour method used by Michaelis et al. [1] for their microscale simulations of the ABL flow over individual leads. Among other methods to diagnostically determine variations of z_i, also the contour method has been originally proposed by Sullivan et al. [2]. By applying the method in the version as described in Michaelis et al. [1], we parametrize z_i as a function of the distance y to the downwind boundary of the inflow region (at $y = 0$ km) by tracking a specific contour line of the potential temperature, whose corresponding vertical position is then set equal to the ABL height z_i. This procedure is repeated at each grid cell in flow direction and for each time step. More detailed explanations are given by Michaelis et al. [1].

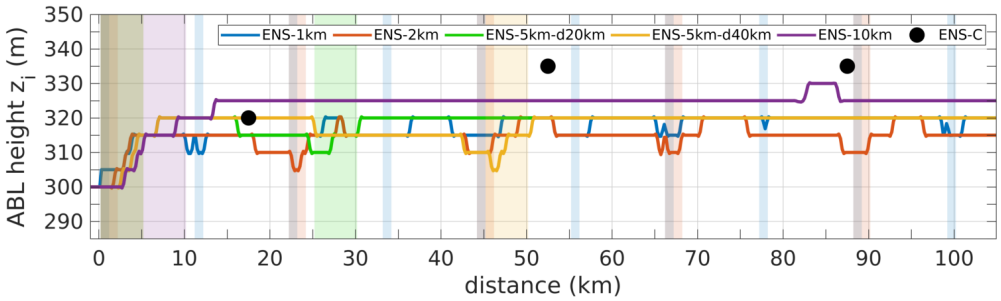

Figure S1. ABL height z_i as a function of distance y to the downwind boundary of the inflow region (at $y = 0$) obtained by the model runs NL-M20-zi for the lead-resolving cases ENS-1km, ENS-2km, ENS-5km-d20km, ENS-5km-d40km, and ENS-10km, and by the model run NL-LS96-zi for case ENS-C. Cases and model runs are described in Figure 2 and Table 1 (see Section 2 of the main manuscript). The colored rectangles denote the positions of the leads. The flow is from left to right.

As shown in Figure S1, z_i first increases with increasing distance for all cases. This is due to the sudden warming over the lead surfaces (lead-resolving cases) or over the surface with 91% sea ice cover (case ENS-C) once the ABL flow crosses the downwind edge of the inflow regions with 100% sea ice at 0 km distance. For the lead-resolving cases, three features are obvious. First, the wider the lead is, the higher is also the maximum height to which z_i increases. Thus, for case ENS-10km, we obtain a maximum of 330 m for z_i. Second, z_i is more or less at a constant level in the leads' downwind regions. Third, for the lead-resolving cases with more than one lead, z_i mostly slightly decreases upwind

of the leads downwind of the corresponding one further upwind. Note that such a slight decrease of the ABL height upwind of individual leads was also indicated by the LES and small-scale model results of Michaelis et al. [4], who also considered simulations of an idealized, lead-perpendicular ABL flow over leads.

For case ENS-C, z_i also increases with increasing distance y (Figure S1). While for the grid cell closest to the inflow edge the corresponding value is in the range of the values obtained for the other cases, z_i increases to 335 m further downwind in the simulation of this case. This is higher than shown by the simulations of all lead-resolving cases.

2. Results from Additional Model Simulations

In the following Figures S2–S7 and Tables S1 and S2, we show the simulations results of the model runs using the local mixing-length closure (model runs MIX for all cases) or using the non-local closures with a fixed value for the ABL height z_i (model runs NL-M20 for the lead-resolving cases and run NL-LS96 for case ENS-C). The corresponding results from the model runs using the non-local closures with variable z_i are shown in Figures 3–5 and Table 2 in the main manuscript. All model runs and cases are described there in Section 2.

Figure S2 shows the potential temperature and horizontal wind speed as a function of distance and height over the six different domains as obtained by the model runs MIX and thus using the local mixing-length closure. In Figure S3, the corresponding results are shown from the model runs NL-M20 for the lead-resolving cases and from the model run NL-LS96 of the case ENS-C. As in Figure 3 of the main manuscript, Figures S2 and S3 show potential temperatures as deviations from the inflow potential temperature of 250 K and wind speeds as dimensionless values normalized by the ABL-averaged inflow wind speed of 5 ms^{-1}.

Figures S4–S7 show the turbulent fluxes of heat and momentum as a function of distance at 10 m and 300 m height as obtained either by the model runs MIX (Figures S4 and S5) or by the model runs using the non-local closures with constant z_i (runs NL-M20 for the lead-resolving cases and run NL-LS96 for case ENS-C, Figures S6 and S7).

In Table S1, we show the values of selected characteristic quantities derived from the domain-averaged vertical profiles shown in Figures 6a,d and 7a,d in the main manuscript (model runs MIX). In Table S2, we show the corresponding values derived from Figures 6b,e and 7b,e in the main manuscript (model runs NL-M20 for the lead-resolving cases and run NL-LS96 for case ENS-C).

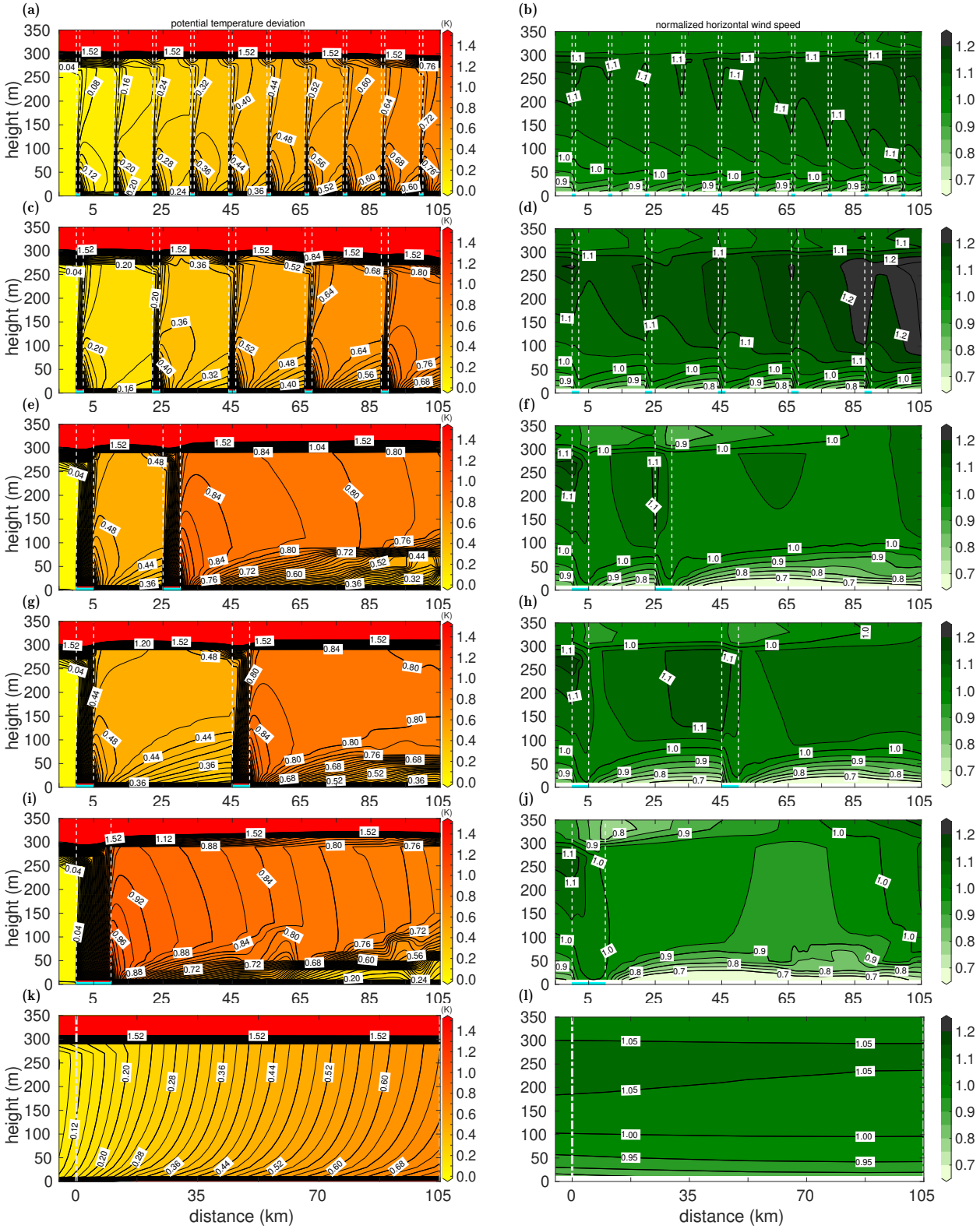

Figure S2. Deviation of potential temperature from the ABL-averaged inflow potential temperature (250 K) and horizontal wind speed normalized by the ABL-averaged inflow wind speed (5 ms^{-1}) as functions of height and distance to the downwind edge of the inflow region at 0 km as in Figure 3 in the main manuscript, but results are shown from the model runs MIX for both the lead-resolving cases (ENS-1km (**a**,**b**), ENS-2km (**c**,**d**), ENS-5km-d20km (**e**,**f**), ENS-5km-d40km (**g**,**h**), and ENS-10km (**i**,**j**)) and for case ENS-C (**k**,**l**). Cases and model runs are described in Figure 2 and Table 1 (see Section 2 of the main manuscript).

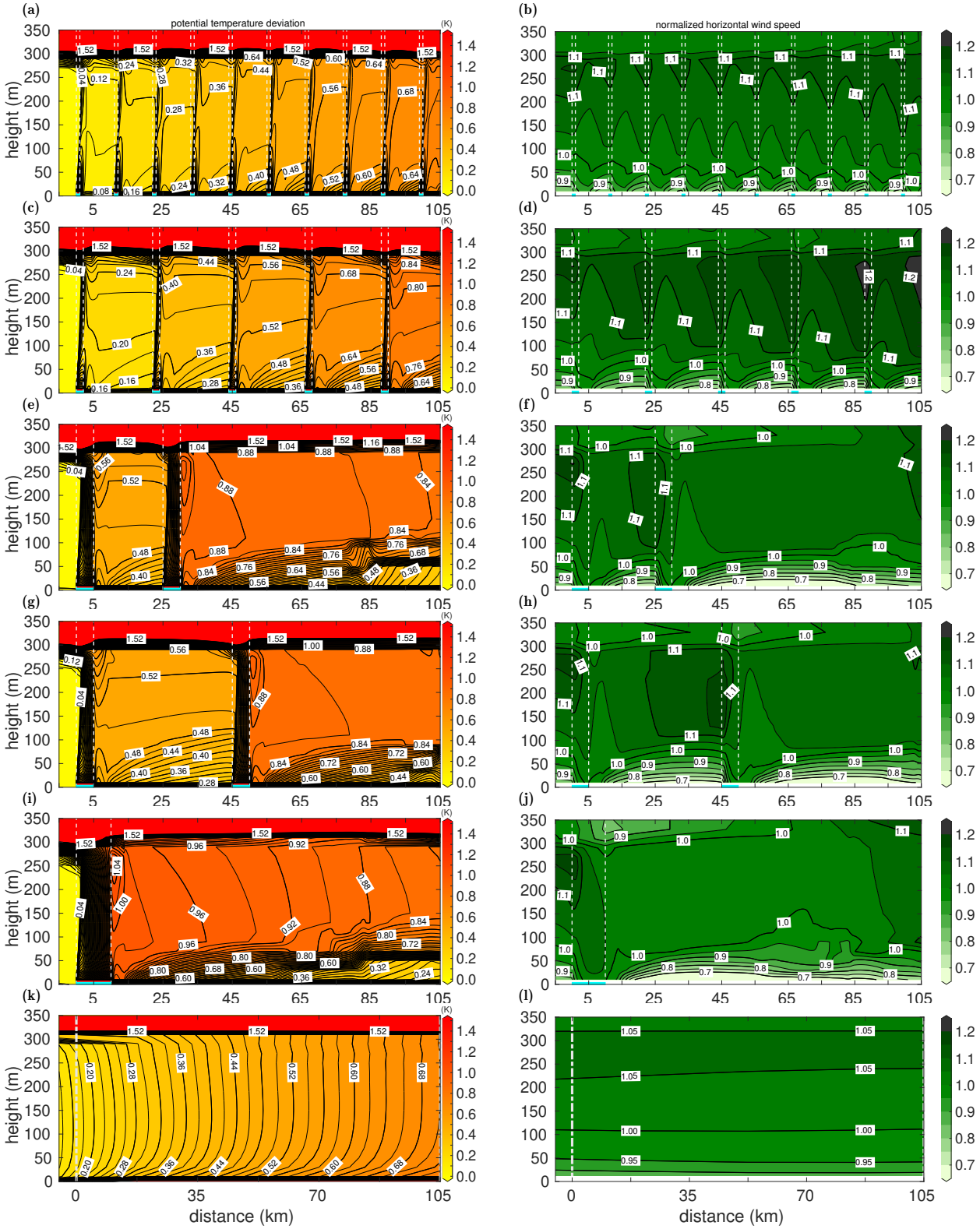

Figure S3. Deviation of potential temperature from the ABL-averaged inflow potential temperature (250 K) and horizontal wind speed normalized by the ABL-averaged inflow wind speed (5 ms^{-1}) as functions of height and distance to the downwind edge of the inflow region at 0 km as in Figure 3 in the main manuscript, but results are shown from the model runs NL-M20 for the lead-resolving cases (ENS-1km (**a**,**b**), ENS-2km (**c**,**d**), ENS-5km-d20km (**e**,**f**), ENS-5km-d40km (**g**,**h**), and ENS-10km (**i**,**j**)) and from the model run NL-LS96 for case ENS-C (**k**,**l**). Cases and model runs are described in Figure 2 and Table 1 (see Section 2 of the main manuscript).

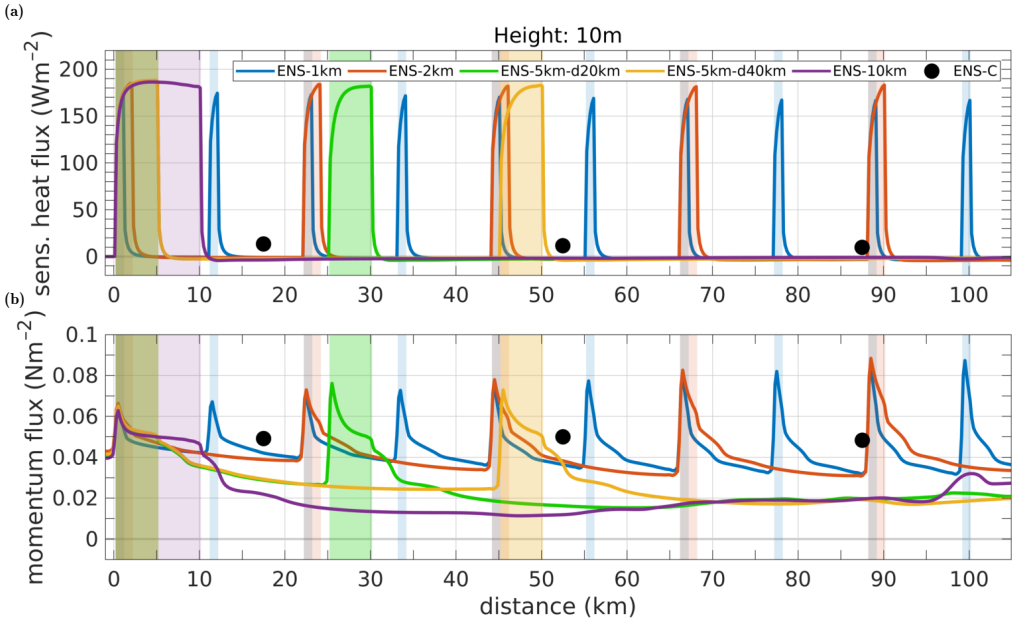

Figure S4. Fluxes of sensible heat (**a**) and momentum (**b**) at height $z = 10$ m as a function of distance as in Figure 4 in the main manuscript, but results are shown from the model runs MIX for all cases. Cases and model runs are described in Figure 2 and Table 1 (see Section 2 of the main manuscript). Modified based on Michaelis [3].

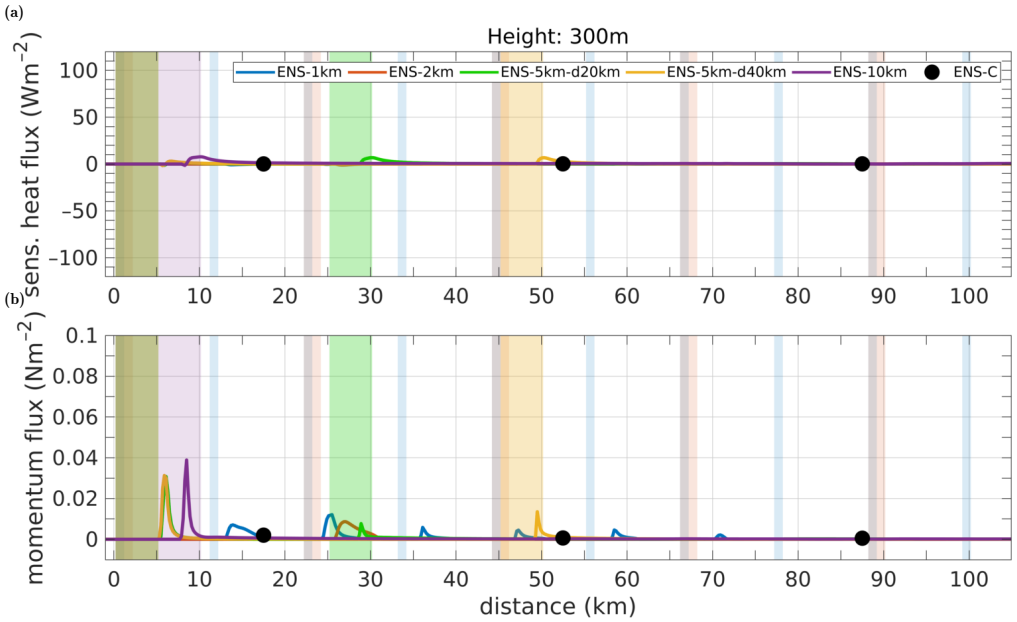

Figure S5. Fluxes of sensible heat (**a**) and momentum (**b**) at height $z = 300$ m as a function of distance as in Figure 5 in the main manuscript, but results are shown from the model runs MIX for all cases. Cases and model runs are described in Figure 2 and Table 1 (see Section 2 of the main manuscript). Modified based on Michaelis [3].

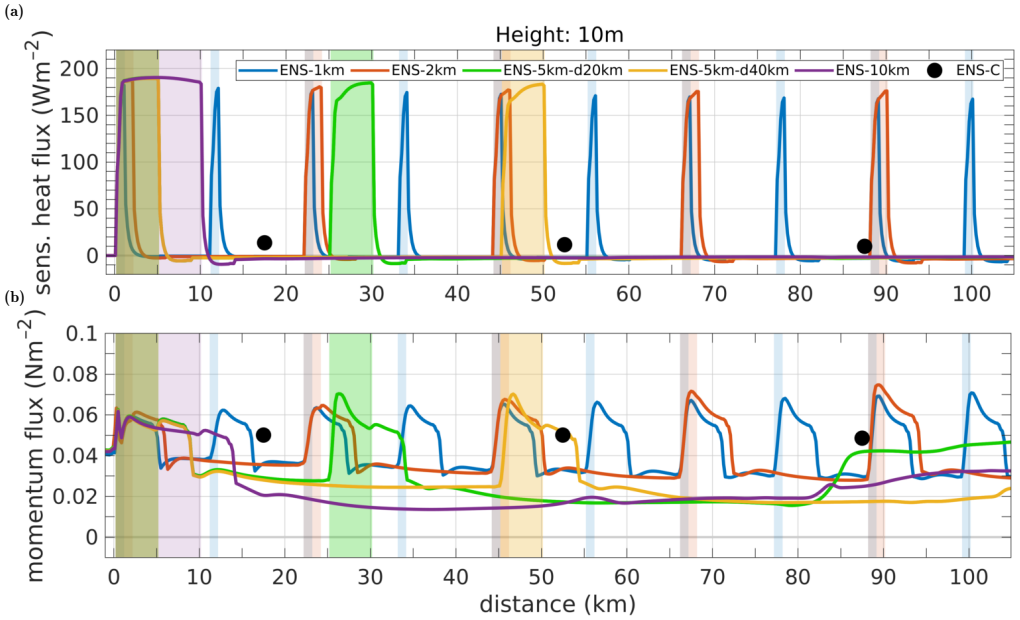

Figure S6. Fluxes of sensible heat (**a**) and momentum (**b**) at height $z = 10$ m as a function of distance as in Figure 4 in the main manuscript, but results are shown from the model runs NL-M20 of the lead-resolving cases ENS-1km, ENS-2km, ENS-5km-d20km, ENS-5km-d40km, ENS-10km and from the model run NL-LS96 for case ENS-C. Cases and model runs are described in Figure 2 and Table 1 (see Section 2 of the main manuscript). Modified based on Michaelis [3].

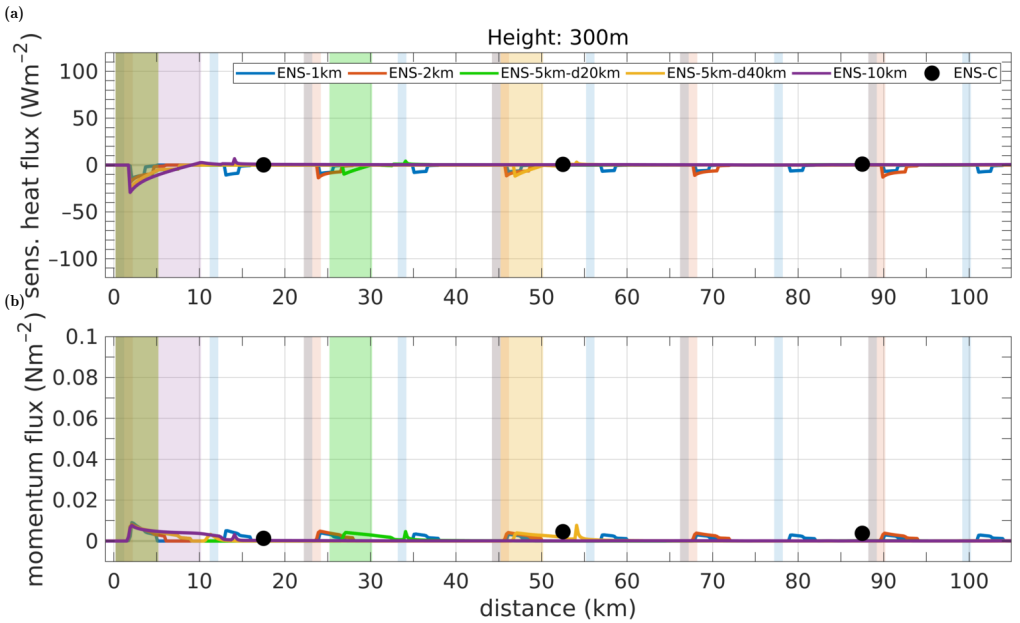

Figure S7. Fluxes of sensible heat (**a**) and momentum (**b**) at height $z = 300$ m as a function of distance as in Figure 5 in the main manuscript, but results are shown from the model runs NL-M20 of the lead-resolving cases ENS-1km, ENS-2km, ENS-5km-d20km, ENS-5km-d40km, ENS-10km and from the model run NL-LS96 for case ENS-C. Cases and model runs are described in Figure 2 and Table 1 (see Section 2 of the main manuscript). Modified based on Michaelis [3].

Table S1. Overview of the domain-averaged values of selected characteristic quantities as in Table 1 in the main manuscript, but results are shown from the model runs MIX for all six cases. Cases and model runs are described in Figure 2 and Table 1 (see Section 2 of the main manuscript).

	Case					
Quantity	**ENS-1km**	**ENS-2km**	**ENS-5km-d20km**	**ENS-5km-d40km**	**ENS-10km**	**ENS-C**
Surface heat flux (Wm^{-2})	13.9	14.3	15.0	15.0	15.8	12.0
Minimum heat flux in ABL (Wm^{-2})	-0.01	-0.04	-0.01	-0.01	-0.01	-0.01
ABL warming (K)	0.40	0.46	0.66	0.60	0.73	0.43
ABL stratification below 100 m ($K(100\,m)^{-1}$)	-0.04	0.01	0.24	0.17	0.36	-0.10
ABL stratification ($K(100\,m)^{-1}$)	0.31	0.41	0.21	0.24	0.18	0.18
Minimum wind speed in ABL above 10 m (ms^{-1})	4.3	4.3	3.5	3.6	3.3	4.3
Maximum wind speed in ABL (ms^{-1})	5.6	5.8	5.3	5.4	4.9	5.3
Surface momentum flux ($10^{-2}Nm^{-2}$)	4.6	4.5	3.0	3.0	2.6	5.1

Table S2. Overview of the domain-averaged values of selected characteristic quantities as in Table 1 in the main manuscript, but results are shown from the model runs NL-M20 for the lead-resolving cases ENS-1km, ENS-2km, ENS-5km-d20km, ENS-5km-d40km, and ENS-10km and from the model run NL-LS96 for case ENS-C. Cases and model runs are described in Figure 2 and Table 1 (see Section 2 of the main manuscript).

	Case					
Quantity	**ENS-1km**	**ENS-2km**	**ENS-5km-d20km**	**ENS-5km-d40km**	**ENS-10km**	**ENS-C**
Surface heat flux (Wm^{-2})	13.1	13.8	15.0	15.0	16.0	10.9
Minimum heat flux in ABL (Wm^{-2})	-1.4	-1.6	-0.7	-0.7	-0.6	0.3
ABL warming (K)	0.41	0.47	0.69	0.63	0.79	0.42
ABL stratification below 100 m ($K(100\,m)^{-1}$)	-0.00	0.06	0.28	0.22	0.41	-0.07
ABL stratification ($K(100\,m)^{-1}$)	0.22	0.28	0.18	0.20	0.19	-0.02
Minimum wind speed in ABL above 10 m (ms^{-1})	4.3	4.2	3.7	3.7	3.5	4.3
Maximum wind speed in ABL (ms^{-1})	5.6	5.8	5.5	5.5	5.2	5.4
Surface momentum flux ($10^{-2}Nm^{-2}$)	4.6	4.3	3.2	3.2	2.9	5.2

References

1. Michaelis, J.; Lüpkes, C.; Schmitt, A. U.; Hartmann, J. Modelling and parametrization of the convective flow over leads in sea ice and comparison with airborne observations. *Q. J. Roy. Meteor. Soc.* **2021**, *147*, 914–943. doi: 10.1002/qj.3953
2. Sullivan, P. P.; Moeng, C.-H.; Stevens, B.; Lenschow, D. H.; Mayor, S. D. Structure of the entrainment zone capping the convective atmospheric boundary layer. *J. Atmos. Sci.* **1998**, *55*, 19, 3042–3064. doi: 10.1175/1520-0469(1998)055<3042:SOTEZC>2.0.CO;2
3. Michaelis, J. Modelling and parametrization of turbulent convective processes over leads in sea ice. PhD thesis, Universität Bremen, Germany, 2020. doi: 10.26092/elib/428
4. Michaelis, J.; Lüpkes, C.; Zhou, X.; Gryschka, M.; Gryanik, V. M. Influence of lead width on the turbulent flow over sea ice leads: Modeling and parametrization. *J. Geophys. Res.-Atmos.* **2020**, *125*, 15, e2019JD031996. doi: 10.1029/2019JD031996